A Stochastic Approach for Recovery Times of Coastal Dune Vegetation

Geophysical Research Letters

RESEARCH LETTER
10.1029/2026GL123322

A Stochastic Approach for Recovery Times of Coastal Dune Vegetation

D. Demichele[1] and **C. Camporeale**[1]

[1]DIATI, Department of Environment, Land and Infrastructure Engineering, Politecnico di Torino, Turin, Italy

Key Points:

- A closed-form analytical expression of recovery time of coastal dune vegetation is derived
- Recovery time is primarily controlled by the equilibrium vegetation cover under stochastic forcing
- Recovery times varies sharply along the cross-shore coordinate

Supporting Information:

Supporting Information may be found in the online version of this article.

Correspondence to:

D. Demichele,
davide.demichele@polito.it

Citation:

Demichele, D., & Camporeale, C. (2026). A stochastic approach for recovery times of coastal dune vegetation. *Geophysical Research Letters*, *53*, e2026GL123322. https://doi.org/10.1029/2026GL123322

Received 31 MAR 2026
Accepted 21 JUL 2026

Author Contributions:

Conceptualization: D. Demichele
Data curation: D. Demichele
Formal analysis: D. Demichele
Funding acquisition: C. Camporeale
Investigation: D. Demichele
Methodology: D. Demichele
Project administration: C. Camporeale
Software: D. Demichele
Supervision: C. Camporeale
Validation: D. Demichele
Visualization: D. Demichele
Writing – original draft: D. Demichele
Writing – review & editing: C. Camporeale

Abstract The resilience of coastal dunes to environmental stress largely depends on vegetation recovery, which promotes sediment trapping and sand stabilization. However, post-disturbance recovery dynamics remain difficult to quantify due to the complex interplay between biotic and abiotic processes. Here, we introduce a novel analytical formulation for vegetation recovery time, defined as the time required to transition from a degraded to an optimal state. The approach is based on a minimal stochastic model that captures environmental variability while remaining computationally efficient, linking recovery dynamics to environmental forcings, dune morphology, and species-specific traits. Steady-state mean vegetation cover, μ_ψ, biomass decay rate k and aeolian integral timescale $\mathcal{T}$ are observed to exert major influence on recovery times. This approach provides a simplified and analytically tractable description of coastal vegetation resilience, offering a basis for assessing ecosystem response under changing environmental forcing.

Plain Language Summary Coastal dunes act as natural barriers against storms and help maintain shoreline stability. Their formation and resilience largely depend on vegetation, which stabilizes sand and supports recovery after disturbances. However, how quickly vegetation recovers after extreme events such as storm surges or hurricanes remains poorly understood. This study introduces a method to estimate vegetation recovery time using stochastic process theory. The approach accounts for the random nature of environmental forcing (wind and waves), as well as dune geometry and plant characteristics. Results show how these factors interact to control recovery rates, providing a practical tool to assess dune resilience and support coastal management under changing climate conditions.

1. Introduction

Coastal dunes provide natural protection against storm impacts and contribute to shoreline stability (Sabo et al., 2024). Their formation and persistence largely depend on vegetation, which promotes sediment trapping and enhances resistance to erosion. However, coastal dune systems are increasingly exposed to disturbances such as storms, sea-level rise, and human activities, which can degrade vegetation cover and destabilize the system, with urbanization alone associated with up to a 12% loss in recreational ecosystem services (Carranza et al., 2019). In this context, the ability of vegetation to recover after disturbance is a key component of dune resilience.

Despite its importance, a general and analytically tractable formulation of vegetation recovery time in coastal dunes is still lacking. Recovery dynamics emerge from the interplay between stochastic environmental disturbances (e.g., wind and wave forcing), sediment transport, and species-specific traits, making them inherently variable in time and space. While observations provide estimates of recovery rates under specific conditions (Brantley et al., 2014; Johnston et al., 2023; Miller et al., 2010; Over & Sherwood, 2025; Zarnetske et al., 2015), a general framework to quantify the time required for vegetation to transition from a degraded to an equilibrium state is still missing. In particular, an analytically tractable formulation that links recovery time to environmental forcing, dune morphology, and biological characteristics is not yet available.

Several modeling frameworks have been developed to describe vegetation–sediment interactions and eco-morphodynamic feedbacks in coastal dune systems. Process-based models resolve coupled hydrodynamic, aeolian, and ecological processes (Charbonneau et al., 2022; Costas et al., 2020), but are often computationally demanding and not well suited for systematic exploration of recovery dynamics. Reduced-complexity and cellular models offer a more tractable alternative (Heminway et al., 2024; Keijsers et al., 2016), but typically rely on empirical formulations that limit direct identification of controlling mechanisms.

Stochastic approaches have been extensively employed to probabilistically describe the spatio-temporal response of a broad range of physical, ecological, and environmental systems subjected to random fluctuations (Boano et al., 2006; Borgogno et al., 2010; Mantelli et al., 2016; Perona et al., 2012; Rodriguez-Iturbe et al., 1999; Tamea et al., 2010). Although several stochastic models have been developed to describe vegetation biomass dynamics, most of them focus on riparian ecosystems (Camporeale & Ridolfi, 2006; Perona et al., 2009), whereas only a limited number of recent studies have addressed coastal vegetation (Adhithya Ramakrishnan & Duran Vinent, 2025; Camporeale & Latella, 2025).

Within these frameworks, threshold-crossing statistics of noise-driven systems constitute a key aspect of the analysis. Among the most widely used quantities is the mean first-passage time (MFPT), defined as the average time required for a stochastic process to reach a prescribed threshold for the first time, starting from an initial state. Analytical expressions for the MFPT have been derived for a variety of stochastic processes and models (Calvani & Perona, 2023; Laio et al., 2001; Tamea et al., 2011).

Despite its relevance, direct applications of the MFPT to vegetation dynamics remain scarce. While some examples are available for riparian vegetation (Vesipa et al., 2016), to the best of our knowledge no analytical formulation has yet been proposed for coastal vegetation.

In this study, we derive a closed-form analytical expression to quantify vegetation recovery time in coastal dune systems. Building upon the stochastic modeling approach proposed in Camporeale and Latella (2025), we formulate recovery as a mean first passage time problem, deriving a closed-form expression for the time required for vegetation to transition from a degraded to an equilibrium state. This formulation provides a direct and tractable link between recovery dynamics and environmental forcing, dune morphology, and species-specific traits.

2. Methods

2.1. Stochastic Modeling

In the following, we briefly summarize the stochastic model proposed by Camporeale and Latella (2025)—hereafter CL25—which forms the basis for the evaluation of vegetation recovery time. For a more comprehensive presentation, the reader is referred to the original work.

Dune morphology is simplified into a one-dimensional cross-section (Figure 1a), consisting of a linear swash zone with slope angle θ_0, followed by a Gaussian-like dune shape represented by dimensionless quantities such as cross-shore coordinate X, dune steepness β and relative roughness ξ, respectively

$$X = \frac{x}{l}, \qquad \beta = \frac{h}{l}, \qquad \xi = \frac{z_0}{l}. \tag{1}$$

According to Figure 1a, h is the dune height, l is its wavelength (i.e., the toe-heel distance), z_0 is the wall roughness height. The dimensionless dune profile $\eta(X)$ is defined with the shoreline at $X = 0$ and the dune crest at $X = 1$

$$\eta(X) = \tan\theta_0 \arctan X + \beta e^{-4(X-1)^2}. \tag{2}$$

Vegetation biomass is represented by the dimensionless ground cover index $\psi(x,t)$—that is, fractional cover per unit area—, evolving under two environmental forcings: (a) wind and (b) wave run-up, both capable of inducing vegetation decay. In the swash zone, vegetation is mainly affected by flood-induced stress (e.g., anoxia or uprooting), while on foredune slopes and in dune slacks it may undergo wind-driven sand scour leading to root exposure or deposition causing burial of plants. According to their response to sand mobilization, coastal plant species can be grouped into two main categories (Maun, 2009). (a) *Type-I* species are poorly tolerant to sand scour and burial and include pioneer species such as *Euphorbia paralias* and secondary species such as *Helichrysum stoechas*. (b) *Type-II* species, on the other hand, are highly tolerant to sediment dynamics; a notable example is *Ammophila arenaria* (marram grass), which exhibits a positive feedback with sand deposition and erosion over a finite range of sediment transport rates.

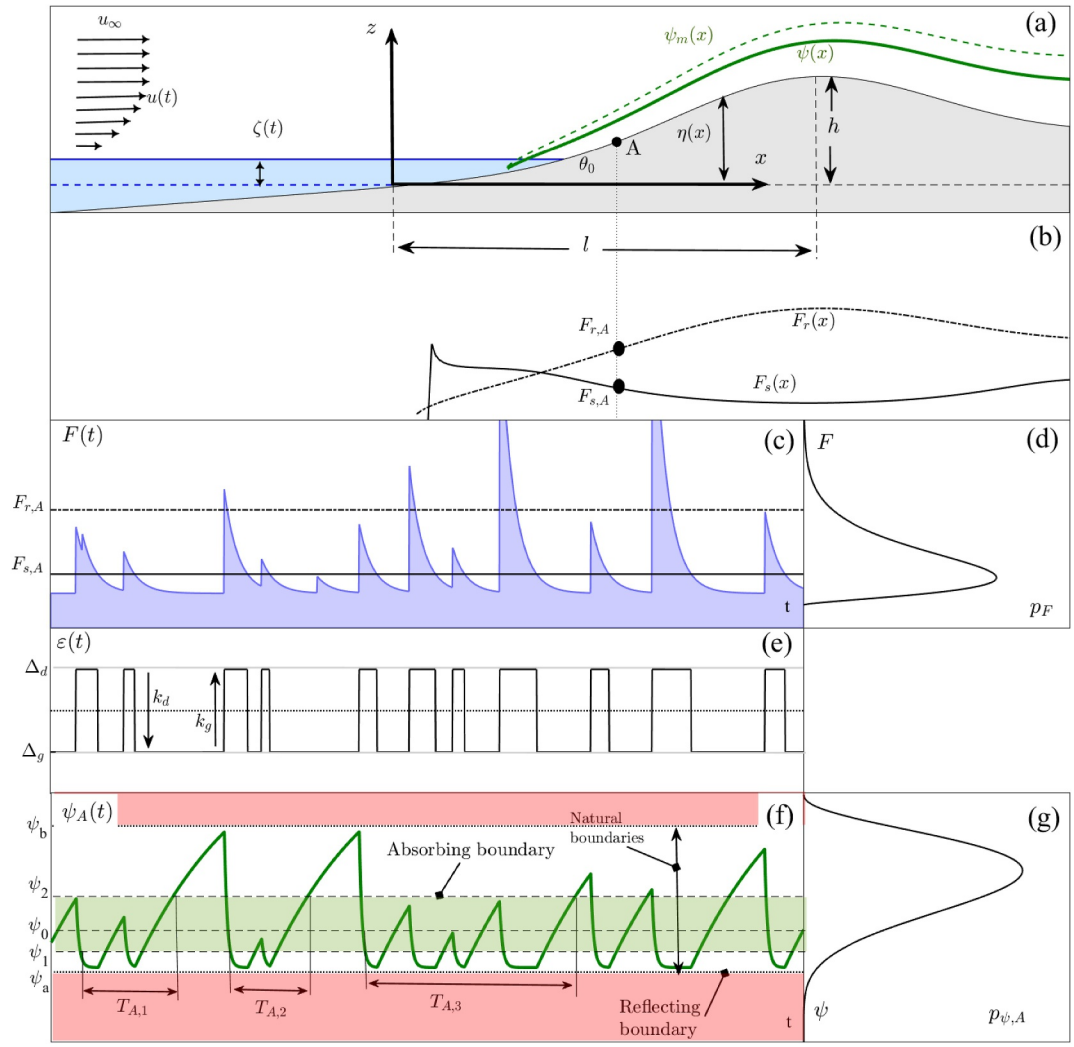

Figure 1. (a) Sketch of a coastal dune cross-section. The solid blue line indicates the water table elevation $\zeta(t)$ relative to mean sea level (dashed blue line). The vertical wind-speed profile $u(t)$ is shown on the left, with u_∞ denoting the free-stream velocity in the atmospheric boundary layer. The solid and dashed green lines represent, respectively, the vegetation cover at a given time and the attainable vegetation cover threshold along the cross-shore direction. (b) Cross-shore distribution of the wave runup threshold F_r (black dot-dashed line) and scour threshold F_s (black solid line). (c–d) Example wind-speed time series and corresponding probability density function, with the thresholds at plot A marked by dot-dashed and solid lines; at plot A, scouring dominates because $F_{s,A} < F_{r,A}$. (e) Time series of the dichotomous noise $\Delta(t)$ at plot A. (f–g) Qualitative vegetation-cover time series at plot A and corresponding probability density function. The sequence of recovery times, $T_{A,i}$, from ψ_0 to ψ_2, is also highlighted.

Both wind and run-up are expressed as a function of the wind velocity at the atmospheric boundary layer u_∞, which is the main stochastic driver, defined by a mean value $\mu_u = \langle u_\infty \rangle$, a coefficient of variation c_u (i.e., standard deviation-to-mean ratio) and an integral timescale $\mathcal{I}_u$ (i.e., the characteristic time over which the values of a fluctuating process remain significantly correlated with themselves).

Recent studies demonstrated how wind can be robustly modeled as a compound Poisson process, consisting of a series of sudden shots having exponentially-distributed inter-arrival times and sizes—with mean values $\mathcal{I}_u c_u^2$ and $\mu_u c_u^2$ respectively—, followed by an exponential decay, with rate $1/\mathcal{I}_u$ (Kang et al., 2024; Rinaldo et al., 2021; Sverdrup & Munk, 1952), as portrayed in Figure 1c. The probability distribution of wind velocity modeled in such a way follows a Gamma-distribution (Figure 1d) (Ridolfi et al., 2011).

It follows that, at any given distance from the shoreline X, biomass experiences alternating periods of random duration of growth and decay (Figure 1f), which is expressed by the simple dimensionless threshold-driven dichotomous model, reading

$$\dot{\psi} = \begin{cases} f_d = -k\psi & F > F_{s|r} \\ f_g = \psi_m - \psi - \alpha & F < F_{s|r} \end{cases} \tag{3}$$

The temporal evolution of the system $\dot{\psi}$ is referred to a dimensionless time t/t_g, with t_g expressing the characteristic growth time-scale of the vegetation. In the model (Equation 3), biomass decay occurs when the dimensionless wind parameter $F = u_\infty/\sqrt{gl}$ exceeds the critical threshold for scouring/flooding $F_{s|r}$, and growth occurs otherwise. The term $k = t_g/t_d$ represents the dimensionless decay rate, with t_g and t_d being vegetation growth and decay timescales; ψ_m is maximum vegetation cover; $\alpha = \mathcal{K}|\dot{\eta}|$, is an additive term representing the tolerance to sand mobilization rate $|\dot{\eta}|$ (Vinent & Moore, 2013), where $\mathcal{K}$ is a species-dependent multiplicative coefficient. The term α accounts for the positive response of *Type-II* species (e.g., Marram grass) to sand erosion and deposition, while, for *Type-I* species, $\alpha = 0$.

The control threshold $F_{s|r}$ is given by the minimum between the scouring threshold F_s and the wave run-up threshold F_r (Figure 1b). The latter depends on dune elevation, tidal range, beach slope, and wave–wind scaling, and is obtained by equating the water elevation reached by wave run-up on the swash zone (Stockdon et al., 2006) to the local topographic elevation $\eta(X)$; in this way, vegetation decay is triggered where the run-up level exceeds the ground elevation. The scouring threshold differs for *type-I* and *type-II* vegetation and accounts for sediment mobility, local slope effects, and vegetation properties. For *type-I* vegetation, F_s is identified by equating the bottom shear stress to the critical threshold for incipient sediment motion, implying that this vegetation type cannot tolerate either erosion or deposition. For *type-II* vegetation, instead, the scouring threshold corresponds to the erosion/deposition rate beyond which vegetation can no longer keep pace with sediment dynamics, and is mathematically obtained by solving the equation $f_g = 0$. By adopting the perturbative theory by Hunt et al. (1988), CL25 showed that the local bottom stress above the dune can be given in terms of Hilbert transform of the local bottom slope. Mathematical details are provided in Text S1 in Supporting Information S1.

According to the theory of stochastic processes (Ridolfi et al., 2011), the two equations model (3) can be combined into a single stochastic ordinary differential equation

$$\dot{\psi} = f(\psi) + g(\psi)\varepsilon(t), \tag{4}$$

where $\varepsilon(t)$ is a dichotomous Markov noise (DMN), switching between two arbitrary values, Δ_d and Δ_g (Figure 1e), whereas $f(\psi)$ and $g(\psi)$ are functions allowing Equation 4 to reduce to either f_d or f_g (Equation 3) for $\varepsilon = \Delta_d$ or $\varepsilon = \Delta_g$, respectively. Without loss of generality, the noise $\varepsilon(t)$ may be assumed to have zero mean, implying that $k_g\Delta_d + k_d\Delta_g = 0$, where $k_d = \tau_d^{-1} = \langle t_{F>F_{s|r}} \rangle^{-1}$ and $k_g = \tau_g^{-1} = \langle t_{F<F_{s|r}} \rangle^{-1}$ are the mean switching rates between the two states, that is, the inverse of the average permanence times in the decay and growth states, respectively (see Text S2 in Supporting Information S1). By setting $\Delta_d = 1$, one arrives to

$$f(\psi) = \frac{-k_g k\psi + k_d(\psi_m - \psi - \alpha)}{k_d + k_g},\ g(\psi) = \frac{k_d(\psi + \alpha - k\psi - \psi_m)}{k_d + k_g} \tag{5}$$

The master equation, solving Equation 4, describes the time-evolution of the plot-specific probability density function of ψ (Kitahara et al., 1980; Pawula, 1977; Van den Broeck & Hänggi, 1984), which tends to a stationary solution at steady-state (for $t \to \infty$), reading (Camporeale & Latella, 2025)

$$p_\psi = \mathcal{N}\frac{(k-1)\psi + \psi_m - \alpha}{\psi^{1-k_d/k}(\alpha + \psi - \psi_m)^{1-k_g}}, \tag{6}$$

where $\mathcal{N}$ is a normalization constant ensuring that the probability density function integrates to unity. From Equation 6, the mean and standard deviation can be readily obtained by simple integration.

$$\mu_\psi = \int_0^{\psi_m-\alpha} p_\psi \psi d\psi \tag{7}$$

$$\sigma_\psi = \int_0^{\psi_m-\alpha} p_\psi (\psi - \mu_\psi)^2 d\psi \tag{8}$$

2.2. Recovery Time

The computation of the recovery time is based on the theory of MFPT in a bi-stable dynamical system driven by dichotomous Markov noise (Equation 4).

Considering an interval (ψ_1, ψ_2) out of the possible values of the stochastic variable $\psi(t)$, if initially $\psi = \psi_0 \in (\psi_1, \psi_2)$, the MFPT, $T(\psi_0)$, is the expected time for the ψ to cross the domain boundaries (ψ_1, ψ_2) for the first time (Figure 1f).

From the backward Kolmogorov equation associated with the Markovian process described by (4), one can derive the first-exit-time probability density for trajectories starting at ψ_0 and leaving the interval (ψ_1, ψ_2) at a time t (Laio et al., 2001; Van den Broeck & Hänggi, 1984). Its first moment, corresponding to the MFPT, satisfies the equation (Stratonovich, 1967)

$$\Gamma_x^+ T(\psi_0) = -1, \tag{9}$$

where Γ_x^+ denotes the adjoint, or backward, Kolmogorov operator. This operator governs the backward temporal evolution of the probability density function p_ψ (Sancho, 1985; Van den Broeck & Hänggi, 1984).

To determine the MFPT for trajectories exiting the interval through the upper boundary ψ_2, Equation 9 is solved subject to the boundary conditions

$$\left.\frac{\partial T(\psi_0)}{\partial \psi_0}\right|_{\psi_0 \to \psi_a} = 0; T(\psi_0 = \psi_2) = 0$$

where $\psi_a = 0$ is the lower natural boundary of the system. The former represents a "reflecting" boundary at $\psi = \psi_a$, meaning ψ cannot cross ψ_a, whereas the latter means that the MFPT vanishes for trajectories started at ψ_2, acting as an "absorbing" boundary. Under these conditions, the solution of Equation 9 reads (Sancho, 1985)

$$T(\psi_0) = \int_{\psi_0}^{\psi_2} \frac{(k_d + k_g)\, d\psi}{\Xi(\psi)\Psi(\psi)} \int \Psi(\psi')\, d\psi' \tag{10}$$

where

$$\Psi(\psi) = \frac{e^{\int^{\psi} \frac{(k_d+k_g) f(\psi')}{\Phi(\psi')} d\psi'}}{f(\psi) + \Delta_d g(\psi)} = -\frac{1}{k} \psi^{-\left(\frac{k_d}{k}-1\right)} (\alpha + \psi - \psi_m) \tag{11}$$

and

$$\Xi(\psi) = [f(\psi) + \Delta_d g(\psi)]\,[f(\psi) + \Delta_g g(\psi)] = k\psi(\psi_m - \psi - \alpha) \tag{12}$$

Finally, by substituting (12) and (11) into (10), we obtain the exact analytical expression for the MFPT.

$$T(\psi_0) = \frac{(k_d + k_g)\psi}{k_d (\psi_m - \alpha)^3} {}_3F_2\left[\left(1, 1, 1 + \frac{k_d}{k} + k_g\right); \left(2, 1 + \frac{k_d}{k}\right); \frac{\psi}{(\psi_m - \alpha)}\right]\Bigg|_{\psi_0}^{\psi_2}, \tag{13}$$

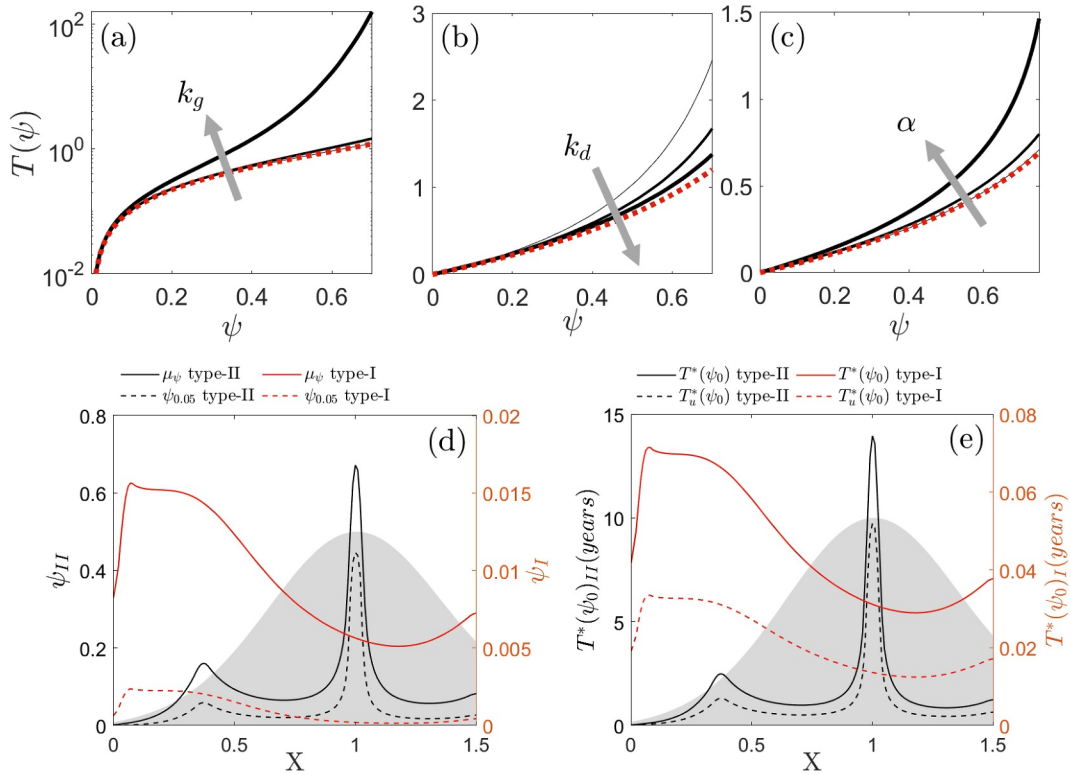

Figure 2. (a–c) Sensitivity of the function $T(\psi)$ with respect to the parameters $k_g = \{10^{-1}, 10^0, 10^1\}$, $k_d = \{10^2, 10^3, 10^4\}$, and $\alpha = \{0, 0.05, 0.2\}$. Red dotted lines indicate the recovery time in undisturbed conditions, $T_u(\psi)$. (d) Spatial distribution of mean vegetation cover μ_ψ (corresponding to ψ_2, solid lines) and fifth percentile of the stationary probability density function $\psi_{0.05}$ (corresponding to ψ_0, dashed lines). (e) Spatial distribution of dimensional recovery time under disturbed conditions (solid lines) and undisturbed conditions (dashed lines). In panels (d–e), *type-I* plots are marked with red color, while *type-II* are marked with black color. The shaded gray area in the background represents the foredune cross-section. The following parameters are used: geometrical parameters $\{\beta, \tan\theta_0, \xi\} = \{0.1, 0.05, 10^{-5}\}$, wind parameters $\{\mu_F, c_F, \mathcal{T}\} = \{0.2, 1, 2/t_g\}$, wave parameters $\{a/l, r\} = \{0, 0.05\}$, ecological parameters for *type-I* (*Euphorbia paralias*) $\{t_g, t_d, \psi_m, \mathcal{K}\} = \{3.5$ yrs; 1; 1; 1$\}$, ecological parameters for *type-II* (*Ammophila arenaria*) $\{t_g, t_d, \psi_m, \mathcal{K}\} = \{7.5$ yr., 1 day, 1, 1$\}$.

where ${}_pF_q[(a_1, \ldots, a_p); (b_1, \ldots, b_q), z]$ is the generalized hypergeometric function (Abramowitz & Stegun, 1968; Levelt, 1961), converging in the interval $(0, \psi_m - \alpha)$. In the following, the recovery time is evaluated as MFPT, starting from ψ_0 equal to the fifth percentile of the stationary probability density function (Equation 6) to $\psi_2 = \mu_\psi$, the steady-state mean vegetation cover (Figure 2d). The former is representative of a degraded vegetation state (e.g., caused by an extreme climatic event), while the latter can be reasonably considered a proxy for optimal biomass conditions at a given distance from the shoreline X and local environmental conditions.

To assess the validity of the analytical formulation, we compared recovery times obtained from Equation 13 with those computed by direct numerical simulations of Equation 3 over a range of parameter configurations. The two approaches show excellent agreement, with an average relative error below 7% (see Figure S1 in Supporting Information S1), supporting the internal consistency of the MFPT-based solution.

3. Results and Discussion

3.1. Exploratory Analysis on Recovery Time

To isolate the role of stochastic environmental disturbances, it is instructive to evaluate the recovery time RT under idealized *undisturbed* conditions, in which vegetation dynamics are governed solely by the deterministic growth law f_g in Equation 3. In this case, RT can be obtained analytically by direct integration, yielding

$$T_u(\psi_0) = -\ln(\psi_m - \psi - \alpha)\Big|_{\psi_0}^{\psi_2} \tag{14}$$

A key property of this logarithmic dependence is that $T_u(\psi_0)$ undergoes an asymptotic increase as ψ approaches its upper bound (i.e., ψ_m for *type-I* and $\psi_m - \alpha$ for *type-II*). This reflects the progressive slowdown of vegetation growth at higher ψ values. Consequently, even under favorable, disturbance-free conditions, the time required for vegetation to increase from ψ to $\psi + \Delta\psi$ increases rapidly as ψ approaches its equilibrium level.

In Figures 2a–2c, we show the sensitivity of the primitive function $T(\psi)$ to the parameters appearing in Equation 13, namely k_g, k_d, and α. The explored parameter ranges were identified from simulations of the stochastic model under a set of representative environmental conditions. Figure 2a shows that the $T(\psi)$ curves become progressively steeper as k_g increases, with the effect becoming particularly pronounced for $k_g > 1$ in the higher ranges of ψ values. From a mathematical standpoint, this behavior reflects a property of generalized hypergeometric functions for which $T(\psi)$ tends asymptotically to $\left[\psi/(\psi_m - \alpha) - 1\right]^{-k_g}$ when the argument approaches 1 (Slater, 1966). On the other hand, a physical interpretation can be obtained by noting that the dimensional shifting rate is $k_g^* = 1/\tau_g^*$—the asterisk denotes we are dealing with dimensional quantities. Since time has been non-dimensionalized using the characteristic growth time, t_g, the dimensionless shifting rate becomes $k_g = \tau_g^{-1} = t_g/\tau_g^*$. Consequently, the condition $k_g > 1$, implies that the mean residence time in the growth state is shorter than the characteristic growth time. Under these conditions, on average, the permanence time in the growth state becomes insufficient for the system to complete its characteristic evolution, causing $T(\psi)$ to increase sharply as ψ approaches its upper bound. Furthermore, k_g is proportional to the probability of vegetation being in the decay state (Ridolfi et al., 2011). As a result, larger values of k_g—associated with harsher environmental conditions—lead to longer average times required to reach a given vegetation state ψ. Conversely, increasing k_d produces flatter $T(\psi_0)$ curves (Figure 2), as it enhances the residence time in the growth state, thereby accelerating recovery. Consistently, Figures 2a and 2b show that, in the limit $k_g \to 0$ (or equivalently $k_d \to \infty$), the curves converge to the undisturbed case. Figure 2c illustrates that increasing $\alpha = \mathcal{K}\langle d\eta/dt\rangle$ leads to longer recovery times, indicating that sand mobilization inhibits vegetation growth. Although, as discussed above, sediment transport may locally promote biomass growth—particularly in *type-II* vegetation—it overall acts as a stressor that both slows recovery and reduces the maximum attainable vegetation cover.

As an example of the application of the proposed method (Figure 3e), we consider the spatial variation of dimensional recovery times $\left(T^*(\psi_0) = t_g T(\psi_0)\right)$ along the cross-shore direction of two different species, *Ammophila arenaria* and *Euphorbia paralias*, which are very common on Mediterranean coastal dunes (Belcore et al., 2021; Bertacchi, 2017; Demichele et al., 2025). As already remarked above, *Euphorbia paralias* is considered *type-I* vegetation, while *Ammophila arenaria* is considered *type-II*. Typical time scales for reaching a fully developed state are 5–10 years for *Ammophila* (Van Der Putten & Kloosterman, 1991) and 2–5 years for *Euphorbia* (Velvin & Embling, 2014). Accordingly, average values of 7.5 and 3.5 years were adopted as characteristic growth time scales t_g in the calculations.

First, Figure 2e shows a significant difference in recovery timescales between the two species. Indeed, despite *Euphorbia* being more susceptible to environmental stressors, resulting in longer residence times in the decay state and thus inhibited growth, the time required to reach the reference equilibrium state $\psi_2 = \mu_\psi$ is 1–2 orders of magnitude shorter than for *Ammophila* ($\approx$1 month at its peak point, compared with $\approx$10 years at the peak point for *Ammophila*). This difference is partly explained by the shorter intrinsic growth time scale t_g of *Euphorbia*. More importantly, under identical environmental conditions, $T^*(\psi_0)$ primarily scales with the target vegetation cover μ_ψ, which is significantly lower for *Euphorbia* than for *Ammophila*, as shown in Figure 2d. In other words, although the growth rate of *Euphorbia* is lower (i.e., lower τ_g or equivalently, higher k_g), the reduced maximum attainable biomass results in a substantially shorter overall recovery time, within a monthly timescales (see Figure S3 in Supporting Information S1).

Another notable feature is that the spatial distribution of $T^*(\psi_0)$ (Figure 2e) closely follows that of μ_ψ (Figure 2d). This correspondence suggests that μ_ψ, that is, the exit point of the temporal trajectory of ψ, is the primary quantity controlling the recovery time. This relationship will be discussed in more detail later on.

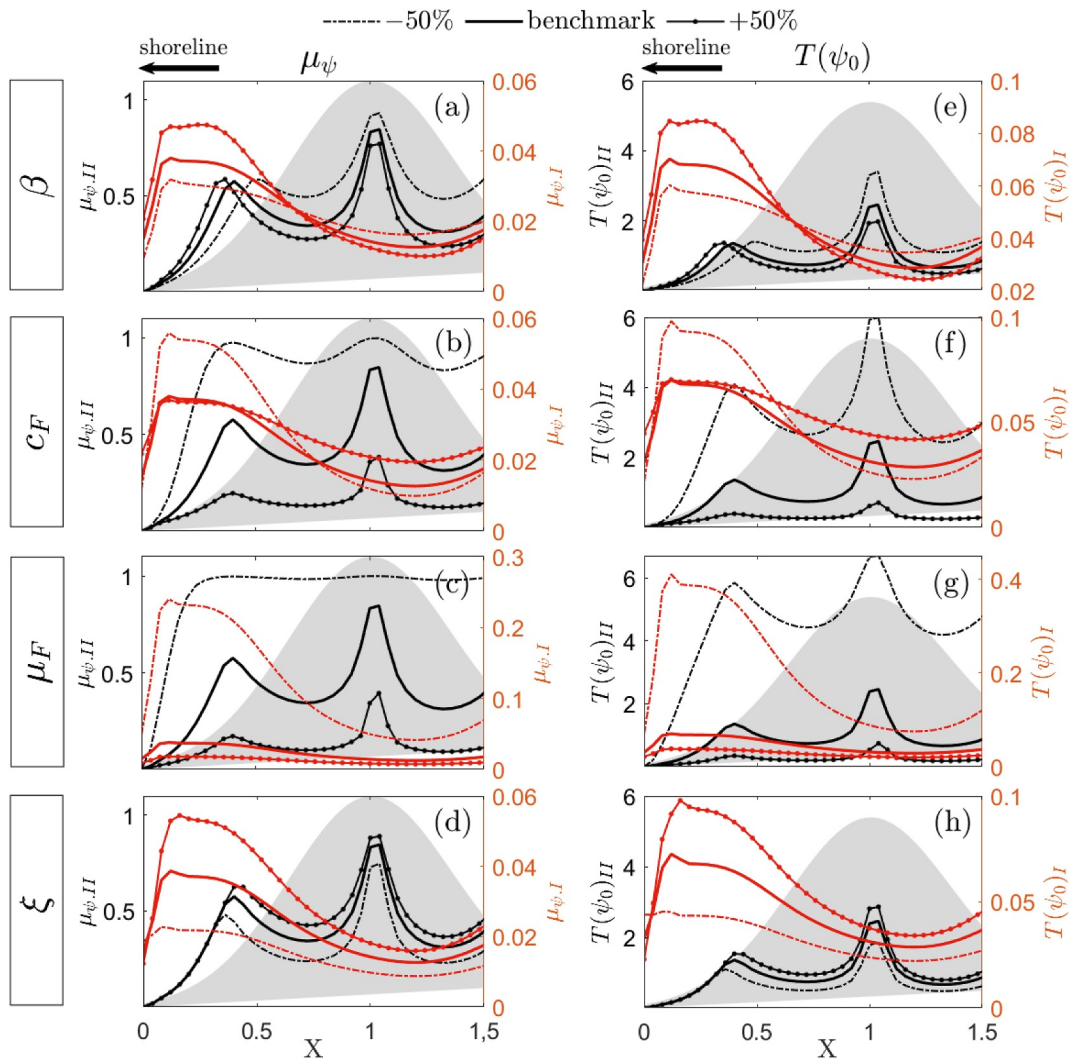

Figure 3. Comparative sensitivity analysis of μ_ψ (left column) and $T(\psi_0)$ (right column) to the main model parameters. Each parameter is varied individually by ±50% relative to the benchmark set $\{\beta, \mu_F, c_F, \xi\} = \{0.1, 0.2, 1, 10^{-5}\}$. (a–b) Sensitivity to β. Plots referred to *Type-I* vegetation are marked with red color, while *type-II* are marked with black color and the shaded gray area in the background represents a foredune cross-section. In all panels, right y-axis are referred to *type-I*, while left y-axis are referred to *type-II*. (a, e) Sensitivity to dune steepness β. (b, f) Sensitivity to wind velocity coefficient of variation c_F. (c, g) Sensitivity to mean wind velocity μ_F. (d, h) Sensitivity to relative roughness ξ. Results computed using the benchmark parameter set are plotted using solid lines, while results computed with increased and decreased parameters by 50% are represented respectively with dotted and dashed lines. Other parameters remains constant for all simulations: $\{\tan\theta_0, \mathcal{T} = \mathcal{I}_u/t_g, a/l, r, k = t_g/t_d, \psi_m; \mathcal{K}\} = \{0.05, 10^{-2}, 0, 0.05, 20, 1, 1\}$.

Lastly, under undisturbed conditions, the recovery time of *Euphorbia* is approximately half that obtained in the presence of random forcing over the entire domain. For instance, $T^*(\psi_0)/T_u^*(\psi_0) \approx 2$ both at the maximum ($X = 0.1$) and at the minimum ($X = 1.2$) of the profile. *Ammophila*, on the other hand, exhibits a similar behavior only in regions sufficiently far from the dune crest ($X < 0.9$ and $X > 1.1$), where $T^*(\psi_0)/T_u^*(\psi_0) \approx 2$. Near the crest ($X \approx 1$), this ratio decreases to approximately 1.5. This reduction is due to the larger values of $F_s|_r$ attained in this region, which decrease the probability of threshold exceedance and, consequently, reduce the shifting rate k_g. As a result, the system dynamics become progressively closer to those of the undisturbed case, as also shown in Figure 2a.

3.2. Sensitivity Analysis

Following CL25, we examined, comparatively, the sensitivity of the recovery times and mean vegetation cover to four independent controlling variables, namely, the dune aspect ratio β, mean non-dimensional wind velocity $\mu_F = \mu_u/\sqrt{gl}$, wind velocity coefficient of variation $c_F = c_u$ and relative roughness ξ. As a reference, we adopt the benchmark configuration $\{\beta, \mu_F, c_F, \xi\} = \{0.1, 0.2, 1, 10^{-5}\}$ and varied each parameter independently by ±50%, while all other parameters remain the same (reported in the caption of Figure 3).

The dependence of $T(\psi_0)$ on the four tested parameters is not explicit, since they do not appear directly in (13). They mainly affect the thresholds $F_{s|r}$, and consequently the shifting rates k_d, k_g, the sand mobilization tolerance α, and the stationary probability density function p_ψ from which $\psi_{0.05}$ and μ_ψ (ψ_0 and ψ_2 respectively) are derived. As a result, k_d, k_g, α, $\psi_0 = \psi_{0.05}$ and $\psi_2 = \mu_\psi$, appearing in the recovery time expression (13) are non-linearly inter-dependent parameters. We refer to Text S1 in Supporting Information S1 for further mathematical details.

In line with results highlighted in the previous section, results portrayed in Figure 3 shows how μ_ψ is the strongest overall controlling parameter on $T(\psi_0)$. For every simulation done with different parameter combinations, the variation caused by the changing of parameters and to spatial distribution of μ_ψ is mirrored by a analogous behavior of $T(\psi_0)$, for both vegetation types.

For instance, increasing β (Figures 3a and 3e) in *type-I* vegetation leads to higher $\mu_\psi - T(\psi_0)$ near the shoreline and in the back-dune slack, while reducing it around the dune crest. For *type-II* vegetation, the effect is more subdued, since β has little influence on the near-shore peak, while slightly reducing $\mu_\psi - T(\psi_0)$ at the dune crest.

Changes in the wind variability, quantified by c_F, produce markedly different responses across vegetation types (Figures 3b and 3f). For *type-I*, a non-monotonic behavior emerges in the near-shore and back-dune regions, where intermediate variability ($c_F = 1$) minimizes $\mu_\psi - T(\psi_0)$ compared to both lower and higher values of c_F. In contrast, at the dune crest, $\mu_\psi - T(\psi_0)$ increases monotonically with c_F. For *type-II*, increasing c_F consistently reduces $\mu_\psi - T(\psi_0)$ across the transect, with a pronounced effect that can nearly halve $T(\psi_0)$ for each increment in c_F (Figure 3f).

Mean wind velocity μ_F also exerts a strong influence on $\mu_\psi - T(\psi_0)$ (Figures 3c and 3g). For both vegetation types, increasing μ_F leads to a substantial reduction of $\mu_\psi - T(\psi_0)$ along the entire transect.

Variations in surface roughness ξ weakly influence $\mu_\psi - T(\psi_0)$ on *type-II* vegetation, compared to *type-I* (Figures 3d and 3h). For both vegetation cases, increasing ξ results in higher $\mu_\psi - T(\psi_0)$.

If considered $T(\psi_0)$ alone, without the reference of μ_ψ, the relation of the recovery time to the parameters may appear counterintuitive. For instance, higher mean wind velocity or its variability (μ_F and c_F) might be expected to increase environmental stress and thus prolong recovery times, yet the results indicate the opposite trend. Similarly, increasing surface roughness ξ, which raises the critical threshold for sediment mobilization and should mitigate stress, might be expected to reduce recovery times, whereas the model predicts an increase. Thus, the spatial behavior of $T(\psi_0)$ is mainly governed by the emergent response of the system, encapsulated in the response variable μ_ψ, rather than by the isolated effects of individual parameters β, μ_F, c_F and ξ.

In contrast, if a fixed threshold is set across the spatial domain ($\psi_2 = cost$), the spatial gradient of $T(\psi_0)$ follows a more straightforward and intuitive trend (see Figure S2 in Supporting Information S1): $T(\psi_0)$ is directly proportional to ψ_2, β, μ_F and c_F, while is inversely proportional to ξ.

The proportionality between μ_ψ and the recovery time $T(\psi_0)$ becomes evident in Figure 4. To highlight this relationship, all results from the sensitivity analysis reported in Figure 3 were combined and plotted in the μ_ψ–$T(\psi_0)$ plane. Remarkably, despite corresponding to different combinations of the parameters $\{\beta, \mu_F, c_F, \xi\}$, the data collapse onto a single curve (red symbols in Figures 4a and 4b). This collapse indicates that μ_ψ is not only the dominant control parameter of the recovery time, but that $T(\psi_0)$ is uniquely determined by μ_ψ for any combination of $\{\beta, \mu_F, c_F, \xi\}$. Consequently, the functional relationship between μ_ψ and $T(\psi_0)$ is invariant with respect to variations of these parameters. Although each data point corresponds to different values of k_d, k_g, α, and μ_ψ, these

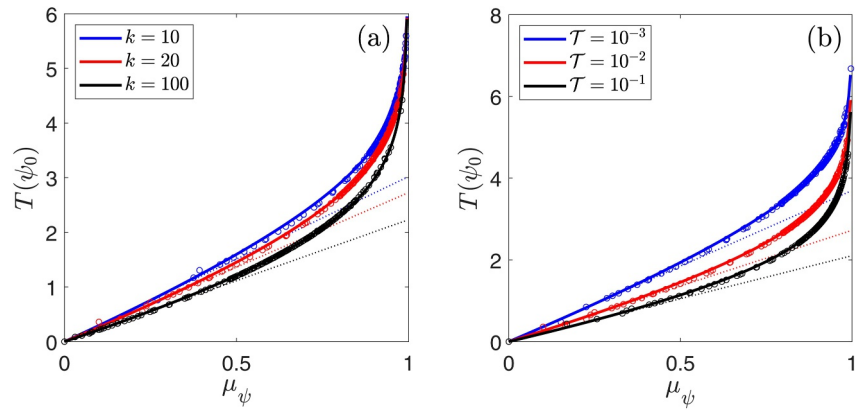

Figure 4. Sensitivity of $\mu_\psi - T(\psi_0)$ curves to the variation of (a) decay rate k and (b) wind velocity integral timescale $\mathcal{T}$. Circular dots represents data collected from simulations using different combinations of $\{\beta, \mu_F, c_F, \xi\}$, used in Figure 3, while fitting curves $T(\psi_0) = a\mu_\psi(1 - \mu_\psi)^{-b}$ are portrayed with solid lines. Each curve is characterized by fixed values of k and $\mathcal{T}$. Dotted lines represent the linear part of the fitting curves $T(\psi_0) = a\mu_\psi$, well-suited to interpolate the data in the lower part of the μ_ψ domain.

quantities are not independent. Their coupled effects combine in such a way that the corresponding recovery times collapse onto the same master curve.

By contrast, the $\mu_\psi - T(\psi_0)$ relationship is sensitive to both the biomass decay rate k and the dimensionless wind integral timescale $\mathcal{T} = \mathcal{I}_u / t_g$, which were kept fixed in the simulations shown in Figure 3. The former represents the main ecological parameter and explicitly appears in Equation 13, whereas the latter directly affects the switching rates (see Text S1 in Supporting Information S1).

Additional simulations performed by varying k and $\mathcal{T}$ reveal that the data no longer collapse onto a single curve, but rather organize into a family of nonlinear curves. These curves are accurately described by the parameterized expression

$$T(\psi_0) = a\mu_\psi(1 - \mu_\psi)^{-b} \tag{15}$$

where a and b depend on k and $\mathcal{T}$. Similar to Equation 13, this expression consists of a linear contribution, $a\mu_\psi$, and a nonlinear correction, $(1 - \mu_\psi)^{-b}$, which produces a vertical asymptote at $\mu_\psi = 1$. A general feature emerging from all simulations is that $T(\psi_0)$ exhibit a marked linear trend in the lower part of the μ_ψ domain, from 0 to $0.4 - 0.5$.

Figure 4a shows that increasing the biomass decay rate k decreases the recovery time for a given value of μ_ψ. At first sight, this result appears counterintuitive, since larger values of k correspond to shorter degradation timescales t_d, implying weaker vegetation resistance and, therefore, one would expect longer recovery times.

Figure 4b further shows that increasing the dimensionless wind integral timescale $\mathcal{T}$ also reduces the recovery time. This behavior also is not immediately obvious. Indeed, larger values of $\mathcal{T}$ correspond to stronger temporal persistence of the wind field and to longer inter-arrival times $(\mathcal{I}_u c_u^2)$ between successive events in the compound Poisson process representing the stochastic forcing.

A physical interpretation of the dependence of $T(\psi_0)$ on the biomass decay rate k can be obtained by noting that increasing k shortens the degradation timescale t_d, thereby making degradation events more abrupt and less persistent. However, in order to reach the same final state μ_ψ, the system compensates through an increase in the degradation switching rate k_d and a decrease in the growth switching rate k_g, effectively increasing the residence time in the growth state (Figure S3 in Supporting Information S1). Consequently, despite the reduced resistance associated with larger values of k, vegetation spends a larger fraction of time recovering, resulting in shorter recovery times.

A similar argument explains the effect of the dimensionless wind integral timescale $\mathcal{T}$. Increasing $\mathcal{T}$ enhances the temporal persistence of the forcing but simultaneously increases the mean inter-arrival time between successive shots. The results indicate that, for the recovery dynamics, the latter effect dominates. As a consequence, disturbances become less frequent and vegetation experiences longer growing periods during which biomass recovery can proceed uninterrupted, leading to shorter recovery times.

4. Conclusions

We developed an analytical description of dune vegetation recovery times under stochastic aeolian forcing. Recovery times are controlled primarily by the steady-state mean vegetation cover μ_ψ, rather than directly by dune morphology or wind statistics. Direct comparison of μ_ψ and $T(\psi_0)$ reveals how their relation is not affected by changing geometrical (β, ξ) or environmental (μ_F, c_F), revealing that μ_ψ acts as an emergent response variable embedding the effects of the external forcing, thus, controlling also the spatial gradients of recovery times at different distances from the shoreline.

Variations in the biomass decay rate k and wind velocity integral timescale $\mathcal{T}$ emerge as controlling parameters of $\mu_\psi - T(\psi_0)$ curves, which remain mostly linear over a broad range of μ_ψ values. Overall, the results indicate that vegetation recovery is governed by the emergent statistics of growth and disturbance periods, providing a low-dimensional description of resilience in stochastic environments.

To illustrate the applicability of the framework under realistic conditions, several U.S. coastal dune systems were analyzed as a proof-of-concept exercise (see Text S3 in Supporting Information S1). In all cases, the spatial distribution of recovery time closely follows that of the equilibrium vegetation cover, confirming the latter as the primary control on recovery dynamics (Camporeale, 2025). Validation is currently limited by the inability of conventional remote sensing products to discriminate vegetation species, whereas recovery time is intrinsically species-dependent. Achieving this level of detail would require either extensive field surveys or higher-resolution observations (e.g., very-high-resolution imagery or UAV-based mapping) (Belcore et al., 2024; Büttelmann, 2022; Demichele et al., 2025; Innangi et al., 2025; Kombiadou et al., 2023), or alternatively the use of advanced remote-sensing techniques such as hyperspectral unmixing (Kombiadou et al., 2025; Medina Machin et al., 2019). Nevertheless, in systems dominated by a single species, recovery times can be more directly linked to observable vegetation patterns (Bonte et al., 2021; Lammers et al., 2024; Pickart, 2021).

Future developments should focus on coupling the present stochastic vegetation model with morphodynamic evolution, thereby linking short-term recovery processes with long-term dune adjustment. In addition, systematic validation through multi-temporal Earth Observation data and targeted field campaigns is needed to constrain species-specific parameters and assess model performance across different coastal settings. Extending the framework to account for mixed-species communities and spatial interactions would further enhance its applicability to real-world ecosystems.

Conflict of Interest

The authors declare no conflicts of interest relevant to this study.

Availability Statement

Matlab scripts and data sets used to generate the results presented in this study are publicly available in the Zenodo repository (Demichele & Camporeale, 2026). The repository includes: (a) a zip file *case_study_data.zip* containing Matlab data sets related to dune geometry, external forcings, and vegetation characteristics for the four case studies analyzed in Section 4 of this manuscript; (b) Matlab script *case_study.m* that generates Figure S5 in Supporting Information S1; (c) Matlab script *RecoveryTime.m* which serves as the main function for computing recovery time distributions in both theoretical and real-case scenarios; (f) Matlab script "numerical_simulation.m" which computes recovery times through direct numerical simulations of the CL25 dichotomous model, used to compare the analytical and numerical approach (see Figure S1 in Supporting Information S1).

Acknowledgments
This study was funded by the European Union (Project Grant Agreement no 101185000–CONCERTO–HORIZON–CL5–2024–D1–01). Views and opinions expressed are however those of the author(s) only and do not necessarily reflect those of the European Union or the European Climate, Infrastructure and Environment Executive Agency (CINEA). Neither the European Union nor the granting authority can be held responsible for them.

References

Abramowitz, M., & Stegun, I. A. (1968). *Handbook of mathematical functions with formulas, graphs, and mathematical tables* (Vol. 55). US Government printing office.

Adhithya Ramakrishnan, K., & Duran Vinent, O. (2025). Modelling the influence of vegetation on the stochastic dynamics of coastal dunes. *Ecohydrology*, *18*(1), e2766. https://doi.org/10.1002/eco.2766

Belcore, E., Latella, M., Piras, M., & Camporeale, C. (2024). Enhancing precision in coastal dunes vegetation mapping: Ultra-high resolution hierarchical classification at the individual plant level. *International Journal of Remote Sensing*, *45*(13), 4527–4552. https://doi.org/10.1080/01431161.2024.2354135

Belcore, E., Pittarello, M., Lingua, A. M., & Lonati, M. (2021). Mapping riparian habitats of natura 2000 network (91e0*, 3240) at individual tree level using UAV multi-temporal and multi-spectral data. *Remote Sensing*, *13*(9), 1756. https://doi.org/10.3390/rs13091756

Bertacchi, A. (2017). Dune habitats of the Migliarino–San Rossore–Massaciuccoli regional park (Tuscany–Italy). *Journal of Maps*, *13*(2), 322–331. https://doi.org/10.1080/17445647.2017.1302365

Boano, F., Revelli, R., & Ridolfi, L. (2006). Stochastic modelling of do and bod components in a stream with random inputs. *Advances in Water Resources*, *29*(9), 1341–1350. https://doi.org/10.1016/j.advwatres.2005.10.007

Bonte, D., Batsleer, F., Provoost, S., Reijers, V., Vandegehuchte, M. L., Van De Walle, R., et al. (2021). Biomorphogenic feedbacks and the spatial organization of a dominant grass steer dune development. *Frontiers in Ecology and Evolution*, *9*, 761336. https://doi.org/10.3389/fevo.2021.761336

Borgogno, F., D'Odorico, P., Laio, F., & Ridolfi, L. (2010). A stochastic model for vegetation water stress. *Ecohydrology: Ecosystems, Land and Water Process Interactions, Ecohydrogeomorphology*, *3*(2), 177–188. https://doi.org/10.1002/eco.120

Brantley, S. T., Bissett, S. N., Young, D. R., Wolner, C. W. V., & Moore, L. J. (2014). Barrier island morphology and sediment characteristics affect the recovery of dune building grasses following storm-induced overwash. *PLoS One*, *9*(8), e104747. https://doi.org/10.1371/journal.pone.0104747

Büttelmann, J. (2022). *Spatio-temporal variability in dune plant communities using UAV and multispectral data*. (Master's thesis). Universidade do Algarve (Portugal). Retrieved from http://hdl.handle.net/10400.1/19360

Calvani, G., & Perona, P. (2023). Splitting probabilities and mean first-passage times across multiple thresholds of jump-and-drift transition paths. *Physical Review E*, *108*(4), 044105. https://doi.org/10.1103/physreve.108.044105

Camporeale, C. (2025). *Dataset and codes inherent to the JGR: Earth surface submission "stochastic dynamics of coastal dune vegetation"*. Zenodo. https://doi.org/10.5281/zenodo.15516692

Camporeale, C., & Ridolfi, L. (2006). Riparian vegetation distribution induced by river flow variability: A stochastic approach. *Water Resources Research*, *42*(10). https://doi.org/10.1029/2006wr004933

Camporeale, C., & Latella, M. (2025). Stochastic dynamics of coastal dune vegetation. *Journal of Geophysical Research: Earth Surface*, *130*(11), e2025JF008610. https://doi.org/10.1029/2025jf008610

Carranza, M. L., Drius, M., Marzialetti, F., Malavasi, M., de Francesco, M. C., Acosta, A. T. R., & Stanisci, A. (2019). Urban expansion depletes cultural ecosystem services: An insight into a Mediterranean coastline. *Rendiconti Lincei. Scienze Fisiche e Naturali*, *31*(1), 103–111. https://doi.org/10.1007/s12210-019-00866-w

Charbonneau, B. R., Duarte, A., Swannack, T. M., Johnson, B. D., & Piercy, C. D. (2022). Doonies: A process-based ecogeomorphological functional community model for coastal dune vegetation and landscape dynamics. *Geomorphology*, *398*, 108037. https://doi.org/10.1016/j.geomorph.2021.108037

Costas, S., Kombiadou, K., & Roelvink, D. (2020). Exploring the role of vegetation and sediment supply to coastal dune states using integrated process-based modelling. In *EGU general Assembly2*. Online. https://doi.org/10.5194/egusphere-egu2020-18568

Demichele, D., Belcore, E., Piras, M., & Camporeale, C. (2025). Species-by-species pattern analysis of coastal dune vegetation. *Journal of Geophysical Research: Biogeosciences*, *130*(2), e2024JG008419. https://doi.org/10.1029/2024jg008419

Demichele, D., & Camporeale, C. (2026). *A stochastic approach for recovery times of coastal dune vegetation*. Zenodo. https://doi.org/10.5281/zenodo.19253142

Heminway, S. S., Cohn, N., Davis, E. H., White, A., Hein, C. J., & Zinnert, J. C. (2024). Exploring ecological, morphological, and environmental controls on coastal foredune evolution at annual scales using a process-based model. *Sustainability*, *16*(8), 3460. https://doi.org/10.3390/su16083460

Hunt, J. C. R., Leibovich, S., & Richards, K. J. (1988). Turbulent shear flows over low hills. *Quarterly Journal of the Royal Meteorological Society*, *114*(484), 1435–1470. https://doi.org/10.1002/qj.49711448405

Innangi, M., Di Febbraro, M., Balsi, M., Colonna, G., Finizio, M., Pontieri, F., & Carranza, M. L. (2025). A novel high-resolution eco-functional vegetation mapping of coastal dunes. *Ecological Indicators*, *171*, 113157. https://doi.org/10.1016/j.ecolind.2025.113157

Johnston, K. K., Dugan, J. E., Hubbard, D. M., Emery, K. A., & Grubbs, M. W. (2023). Using dune restoration on an urban beach as a coastal resilience approach. *Frontiers in Marine Science*, *10*, 1187488. https://doi.org/10.3389/fmars.2023.1187488

Kang, B., Feagin, R. A., Huff, T., & Durán Vinent, O. (2024). Stochastic properties of coastal flooding events – Part 2. *Earth Surface Dynamics*, *12*(1), 105–115. https://doi.org/10.5194/esurf-12-105-2024

Keijsers, J. G. S., De Groot, A. V., & Riksen, M. J. P. M. (2016). Modeling the biogeomorphic evolution of coastal dunes in response to climate change. *Journal of Geophysical Research: Earth Surface*, *121*(6), 1161–1181. https://doi.org/10.1002/2015jf003815

Kitahara, K., Horsthemke, W., Lefever, R., & Inaba, Y. (1980). Exact results for a class of external coloured noise. *Progress of Theoretical Physics*, *64*(4), 1233–1247. https://doi.org/10.1143/ptp.64.1233

Kombiadou, K., Costas, S., Gallego-Fernández, J. B., Yang, Z., Bon de Sousa, L., & Silvestri, S. (2025). Spectral unmixing of coastal dune plant species from very high resolution satellite imagery. *Remote Sensing*, *17*(24), 3991. https://doi.org/10.3390/rs17243991

Kombiadou, K., Costas, S., Yang, Z., & Silvestri, S. (2023). Preliminary results for dune vegetation identification from high-resolution satellite imagery. In *EGU general assembly conference abstracts (pp. EGU-15730)*.

Laio, F., Porporato, A., Ridolfi, L., & Rodriguez-Iturbe, I. (2001). Mean first passage times of processes driven by white shot noise. *Physical Review E*, *63*(3), 036105. https://doi.org/10.1103/physreve.63.036105

Lammers, C., Schmidt, A., van der Heide, T., & Reijers, V. C. (2024). Habitat modification by marram grass negatively affects recruitment of conspecifics. *Oecologia*, *204*(3), 705–715. https://doi.org/10.1007/s00442-024-05525-y

Levelt, A. (1961). Hypergeometric functions I–IV. *Indagationes Mathematicae*, *23*, 397–403.

Mantelli, E., Bertagni, M. B., & Ridolfi, L. (2016). Stochastic ice stream dynamics. *Proceedings of the National Academy of Sciences*, *113*(32), E4594–E4600. https://doi.org/10.1073/pnas.1600362113

Maun, M. A. (2009). *The biology of coastal sand dunes*. Oxford University Press.

Medina Machin, A., Marcello, J., Hernández-Cordero, A. I., Martin Abasolo, J., & Eugenio, F. (2019). Vegetation species mapping in a coastal-dune ecosystem using high resolution satellite imagery. *GIScience and Remote Sensing*, *56*(2), 210–232. https://doi.org/10.1080/15481603.2018.1502910

Miller, T. E., Gornish, E. S., & Buckley, H. L. (2010). Climate and coastal dune vegetation: Disturbance, recovery, and succession. *Plant Ecology*, *206*(1), 97–104. https://doi.org/10.1007/s11258-009-9626-z

Over, J.-S. R., & Sherwood, C. R. (2025). Outwash events inhibit vegetation recovery and prolong coastal vulnerability. *Journal of Geophysical Research: Earth Surface*, *130*(6), e2024JF008162. https://doi.org/10.1029/2024jf008162

Pawula, R. (1977). The probability density and level-crossings of first-order non-linear systems driven by the random telegraph signal. *International Journal of Control*, *25*(2), 283–292. https://doi.org/10.1080/00207177708922228

Perona, P., Daly, E., Crouzy, B., & Porporato, A. (2012). Stochastic dynamics of snow avalanche occurrence by superposition of Poisson processes. *Proceedings of the Royal Society A: Mathematical, Physical and Engineering Sciences*, *468*(2148), 4193–4208. https://doi.org/10.1098/rspa.2012.0396

Perona, P., Molnar, P., Savina, M., & Burlando, P. (2009). An observation-based stochastic model for sediment and vegetation dynamics in the floodplain of an alpine braided river. *Water Resources Research*, *45*(9). https://doi.org/10.1029/2008wr007550

Pickart, A. J. (2021). Ammophila invasion ecology and dune restoration on the west coast of North America. *Diversity*, *13*(12), 629. https://doi.org/10.3390/d13120629

Ridolfi, L., D'Odorico, P., & Laio, F. (2011). *Noise-induced phenomena in the environmental sciences*. Cambridge University Press.

Rinaldo, T., Ramakrishnan, K. A., Rodriguez-Iturbe, I., & Durán Vinent, O. (2021). Probabilistic structure of events controlling the after-storm recovery of coastal dunes. *Proceedings of the National Academy of Sciences*, *118*(1), e2013254118. https://doi.org/10.1073/pnas.2013254118

Rodriguez-Iturbe, I., Porporato, A., Ridolfi, L., Isham, V., & Coxi, D. (1999). Probabilistic modelling of water balance at a point: The role of climate, soil and vegetation. *Proceedings of the Royal Society of London. Series A: Mathematical, Physical and Engineering Sciences*, *455*(1990), 3789–3805. https://doi.org/10.1098/rspa.1999.0477

Sabo, A. B., Cornish, M. R., Castorani, M. C. N., & Zinnert, J. C. (2024). Drivers of dune formation control ecosystem function and response to disturbance in a barrier island system. *Scientific Reports*, *14*(1), 11405. https://doi.org/10.1038/s41598-024-61741-9

Sancho, J. M. (1985). External dichotomous noise: The problem of the mean-first-passage time. *Physical Review A*, *31*(5), 3523–3525. https://doi.org/10.1103/physreva.31.3523

Slater, L. J. (1966). *Generalized hypergeometric functions* (p. 1861). American History.

Stockdon, H. F., Holman, R. A., Howd, P. A., & Sallenger Jr, A. H. (2006). Empirical parameterization of setup, swash, and runup. *Coastal Engineering*, *53*(7), 573–588. https://doi.org/10.1016/j.coastaleng.2005.12.005

Stratonovich, R. L. (1967). *Topics in the theory of random noise* (Vol. 2). CRC Press.

Sverdrup, H. U., & Munk, W. H. (1952). *Wind, sea and swell: The theory of relations for forecasting (No. 303)*. US Government Printing Office.

Tamea, S., Laio, F., Ridolfi, L., & Rodriguez-Iturbe, I. (2011). Crossing properties for geophysical systems forced by Poisson noise. *Geophysical Research Letters*, *38*(18). https://doi.org/10.1029/2011gl049074

Tamea, S., Muneepeerakul, R., Laio, F., Ridolfi, L., & Rodriguez-Iturbe, I. (2010). Stochastic description of water table fluctuations in wetlands. *Geophysical Research Letters*, *37*(6). https://doi.org/10.1029/2009gl041633

Van den Broeck, C., & Hänggi, P. (1984). Activation rates for nonlinear stochastic flows driven by Non-Gaussian noise. *Physical Review A*, *30*(5), 2730–2736. https://doi.org/10.1103/physreva.30.2730

Van Der Putten, W., & Kloosterman, E. (1991). Large-scale establishment of ammophila arenaria and quantitative assessment by remote sensing. *Journal of Coastal Research*, 1181–1194.

Velvin, F. G., & Embling, D. R. (2014). Sea spurge (euphorbia paralias): Using plant development to inform the eradication programme in New Zealand. In *Nineteenth Australasian weeds conference*.

Vesipa, R., Camporeale, C., & Ridolfi, L. (2016). Recovery times of riparian vegetation. *Water Resources Research*, *52*(4), 2934–2950. https://doi.org/10.1002/2015wr018490

Vinent, O. D., & Moore, L. J. (2013). Vegetation controls on the maximum size of coastal dunes. *Proceedings of the National Academy of Sciences*, *110*(43), 17217–17222.

Zarnetske, P. L., Ruggiero, P., Seabloom, E. W., & Hacker, S. D. (2015). Coastal foredune evolution: The relative influence of vegetation and sand supply in the US Pacific Northwest. *Journal of The Royal Society Interface*, *12*(106), 20150017. https://doi.org/10.1098/rsif.2015.0017

References From the Supporting Information

Latella, M., Luijendijk, A., Moreno-Rodenas, A. M., & Camporeale, C. (2021). Satellite image processing for the coarse-scale investigation of sandy coastal areas. *Remote Sensing*, *13*(22), 4613. https://doi.org/10.3390/rs13224613

Sauermann, G., Kroy, K., & Herrmann, H. J. (2001). Continuum saltation model for sand dunes. *Physical Review E*, *64*(3), 031305. https://doi.org/10.1103/physreve.64.031305